# Determination of Atomic Form Factors by means of Coherent Bremsstrahlung

Makoto Tobiyama

Department of Materials Science, Faculty of Science,

Hiroshima University, Higashi-Hiroshima 724, Japan

# Contents

## Abstract

A method has been developed by means of coherent bremsstrahlung from a single crystal for the determination of atomic form factors. This method employs a precise measurement of energy spectra of $\gamma$-rays of several-hundred MeV region produced by 1.2-GeV electrons from single crystals as a function of relative angle between a definite crystal axis and the incident electron beam. It is shown that the spectra contain the electron-screening effect around the target nuclei and give information on the atomic form factor mainly at small momentum transfers. Possible problems with this method have been examined with this experiment using silicon crystal. A method to analyze the experimental results has been established and with this method the deviation of atomic form factor from theoretical calculation is detectable at a level of down to a few %. The present experimental results for silicon crystal are consistent with the form factor obtained by the *Pendellösung* method which shows small deviations from Hartree-Fock model at small momentum transfers. The accuracy attained in this method has been shown not too much affected by the imperfectness of the crystal, at least the dislocation density of up to $10^4 \text{cm}^{-2}$. This method has been applied to an aluminum crystal and it was shown that the experimental results supports the form factor determined by x-ray diffraction; the form factor is deviated at the 111 point by as large as 3.6% from the Hartree-Fock calculation.

3

# 1 Introduction

The atomic form factor is one of the most fundamental quantities in solid state physics. It is a Fourier transform of an electron distribution around a nucleus and bears knowledge of the electron wave function. Precise knowledge of the atomic form factor has also some practical importance as exemplified by the problem associated with the computation of X-ray attenuation coefficients[1]. It is generally impossible to calculate the atomic form factor exactly, because it needs an exact solution for a complicated many-body problem. There are some calculations [2, 3] using approximate methods which are believed to be accurate enough in practical use for some materials. The adequacy of these theoretical treatments, however, should be verified experimentally. Furthermore, it should be noted that the atomic form factor in aggregate may be slightly different from that of an isolated atom. The quality of existing data is inadequate for answering these problems and more detailed measurements have been desired.

Most measurements to determine the atomic form factor performed up to now are mainly by means of X-rays[4] or low-energy electrons[5]. The X-ray experiments are classified into two groups; kinematical and dynamical methods. In the former method, integrated intensities of diffraction images from a single or powder crystal are measured. This method has been applied to many kinds of materials. The most serious problem in the method is that the absolute measurement is not possible and that absorption or extinction corrections are necessary. On the other hand, the absolute value of the form factor is obtainable in the dynamical method. Nevertheless, as the method

4

needs a crystal which is perfect with large dimension, there are few kinds of crystal which are applied in the method. It is therefore highly desirable to develop a new method which is not sensitive to the imperfectness of target crystal.

The photon spectra of coherent bremsstrahlung from high-energy electrons have been found to be very sensitive to the atomic form factor of the target material[6, 7]. This means that a precise measurement of such photon spectra may give us new information on atomic form factors. In addition, the information obtained in this way is complementary to that obtained from X-ray measurements in a sense that the former information reflects the electron screening around nuclei, while the latter directly reflects the electron distribution around nuclei.

In the coherent bremsstrahlung experiment stated above, all the real particles such as the incident and recoil electron and the emitted photon have their momentum of the order of several hundred MeV or higher. As the corresponding wavelength is far smaller than the size of atomic structure and rather closer to the nuclear size, they may be regarded to interact only with the nuclear field. The momentum transfer from incident electron to nucleus, on the other hand, ranges from keV to several hundred MeV. The phonon associated with the atomic vibration can interact with slow electrons surrounding nucleus but not with such high-energy electrons as in the present case. As a result, the phenomenon of our interest is free from any complexity inherent to dynamical treatment of keV electrons[8] and the plane-wave approximation is well valid.

Possible problems in the method using coherent bremsstrahlung are as

5

follows:

- It is generally difficult to measure the energy-spectra of high-energy $\gamma$ rays precisely enough to discuss the small deviation of the spectral shape.

- The method requires considerably complicated experimental technique and long time-consumption. Moreover, there may be no guarantee of the reproducibility for the experimental system in some case.

- By a radiation damage, the target crystal may be broken to some extent.

- The dislocation of the target crystal may heavily affect to the result obtained in the method.

We have already tested the feasibility of the coherent bremsstrahlung method and reported that we could reproduce the shape of the photon spectra for the perfect silicon[9]. As the most precise experiments were made for silicon by measuring *pendellösung* fringes using wedge-shaped crystal[10, 11, 12], silicon crystal may be the most suitable for checking a new method to determine the atomic form factor. We have performed the experiment to clarify the possible problems stated above. We have constructed a new detectors with improved control system. In order to check the reliability of this kind of measurements, we have prepared two kinds of silicon crystal; one is a perfect crystal which is the same one as in the previous experiment and the other is a crystal in which a heavy dislocation has been intentionally introduced.

6

For the metal crystal, as it has free-electrons, the electron distribution may appreciably differ from the model of an isolated atom and its atomic form factor is await for measured with improved accuracy. We therefore have measured the atomic form factor of aluminum crystal by means of coherent bremsstrahlung and compared with the experimental- and theoretical-form factors based on the results obtained in the experiment stated above.

This thesis is organized as follows: Firstly, we briefly describe a theoretical background for coherent bremsstrahlung in section 2. Secondly, in section 3, we give an explanation of the present experimental set-up. Section 4 is devoted to a description of our experimental procedure, data analysis and experimental results. In section 5, the present results for silicon and aluminum crystals are compared with the results of X-ray experiments and also given are the discussions on the validity of the present method and on other related problems. Finally our conclusion is summarized in section 6.

## 2    Coherent Bremsstrahlung

### 2.1    Theoretical foundation

A bremsstrahlung process is diagrammatically represented in Fig. 1, where an electron with energy $E_0$ and momentum $\mathbf{p_0}$ is deflected by the potential shown by a blob and emits a photon with momentum $\mathbf{k}$. Let the energy and momentum of the final state electron be denoted by $E$ and $\mathbf{p}$, respectively, the energy and momentum conservation law read;

$$\mathbf{p_0} = \mathbf{p} + \mathbf{k} + \mathbf{q}, \tag{1}$$
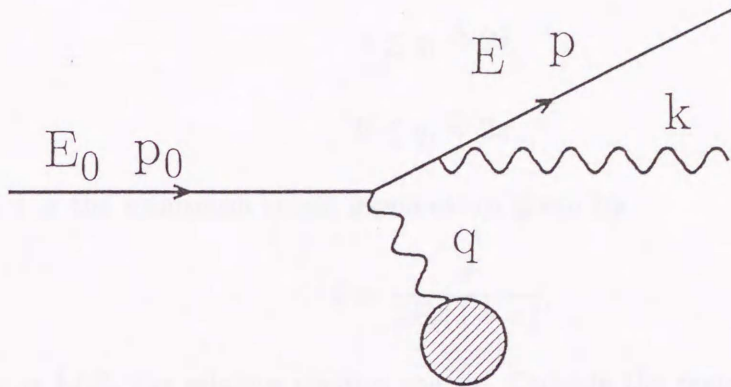
Figure 1: Momentum and angular relations in electron bremsstrahlung. The incident electron momentum, scattered electron momentum, photon momentum and momentum transfer are denoted by $\vec{p_0}$, $\vec{p}$, $\vec{k}$ and $\vec{q}$, respectively.

$$E_0 = E + k, \tag{2}$$

where $\mathbf{q}$ is the recoil momentum of the nucleus. The recoil energy corresponding to $\mathbf{q}$ can be neglected because of the large mass of the recoiling nucleus. Here, and henceforth, we use the natural units in which $m_e = c = \hbar = 1$, where $m_e$ is the electron mass. Conversion of the momentum transfer $\mathbf{q}$ in this natural units to the $[\lambda(\text{Å})^{-1}\sin(\theta/2)]$ unit is accomplished by multiplying a factor 20.60744, which is convenient to represent the momentum transfer in the Rayleigh scattering for the wave length $\lambda$ and the deflection angle $\theta$.

At very high energies where the bremsstrahlung is strongly collimated in the forward direction, $\theta_k \lesssim 1/E_0$, the longitudinal and transverse momentum transfer $q_l$ and $q_t$, respectively, with respect to the incident electron direction

8

are restricted by the relations:

$$\delta \leq q_l \lesssim 2\delta,$$

(3)

$$0 \leq q_t \lesssim 2x,$$

(4)

where $\delta$ is the minimum recoil momentum given by

$$\delta = \frac{x}{2E_0(1-x)},$$

(5)

with $x = k/E_0$ the relative photon energy. Outside the region defined above, the bremsstrahlung is either inhibited or negligibly small.

Though $\delta$ grows rapidly when $x$ approaches unity, it is usually a very small quantity compared to the other momenta involved. Thus, the kinematically allowed region for momentum transfer forms a very thin disc, the "*pancake*" named by Überall, of which the thickness is about $\delta$ and the radius is of the order of unity. It is axially symmetric with respect to the initial electron momentum $p_0$ and it stands at the distance $\delta$ from the origin of the interaction as visualized in Fig. 2.

Using the first order Born approximation, we obtain the Bethe-Heitler expression[13] for the differential cross section for an isolated atom. According to the Bethe-Heitler formalism, the atomic electrons surrounding the nucleus make partial screening of the nuclear charge. This screening effect is represented in terms of the atomic form factor $F(q^2)$, which is the Fourier transform of the charge distribution $\rho(r)$ around the nucleus;

$$F(q^2) = \int e^{i\vec{q}\cdot\vec{r}} \rho(r) d^3r.$$

(6)
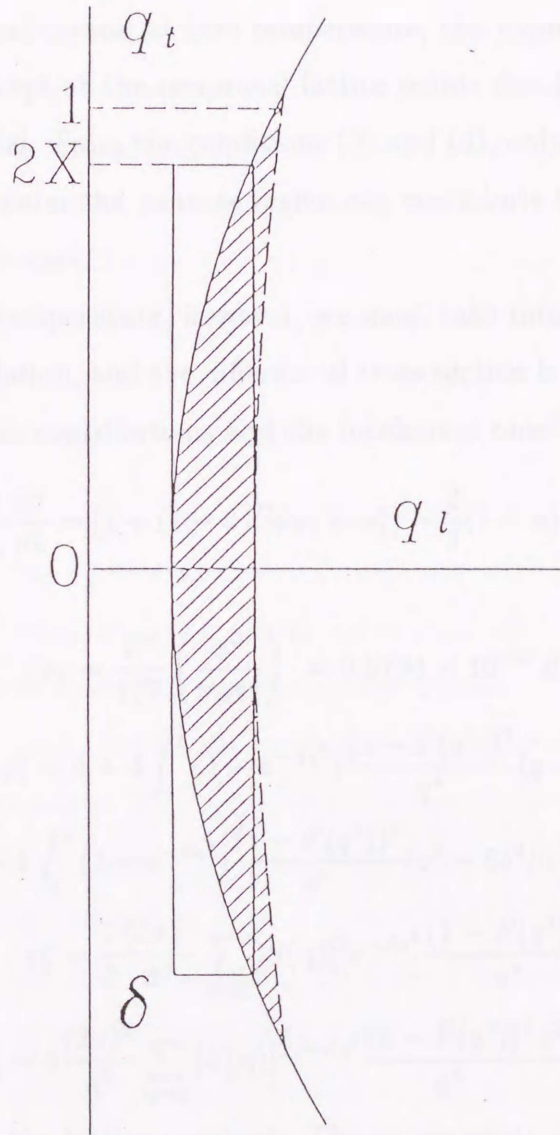
Figure 2: The pancake region (shaded area). Its thickness $\delta$ is far smaller than x or q. The upper kinematical boundary for q is drawn only schematically.

For an ideal crystal at zero temperature, the momentum transfer is not permitted except at the reciprocal lattice points due to the periodic nature of the potential. From the conditions (3) and (4), only the reciprocal lattice points which enter the *pancake* region can contribute to the bremsstrahlung process in this case.

At finite temperature, however, we must take into account the effect of thermal oscillation, and the differential cross section is expressed by the sum of the coherent contributions and the incoherent ones[14];

$$\frac{k}{\sigma_0}\frac{d\sigma}{dk} = [1 + (1-x)^2](\psi_1^i + \psi_1^c) - \frac{2}{3}(1-x)(\psi_2^i + \psi_2^c), \qquad (7)$$

where

$$\sigma_0 = \frac{Z^2}{137}\left(\frac{e^2}{m_e c^2}\right)^2 = 0.5794 \times 10^{-27} Z^2 cm^2,$$

$$\psi_1^i = 4 + 4\int_\delta^1 (1 - e^{-Aq^2})\frac{(1 - F(q^2))^2}{q^4}(q - \delta)^2 q dq,$$

$$\psi_2^i = \frac{10}{3} + 4\int_\delta^1 (1 - e^{-Aq^2})\frac{(1 - F(q^2))^2}{q^4}(q^2 - 6\delta^2 ln\frac{q}{\delta} + 3\delta^2 - 4\frac{\delta^3}{q})q dq,$$

$$\psi_1^c = \frac{1}{2}\frac{(2\pi)^2}{a^3}\sum_{\mathbf{q}=\mathbf{g}}|S(\mathbf{q})|^2 e^{-Aq^2}\frac{(1 - F(q^2))^2}{q^4}\frac{\delta q_t^2}{q_l^2}$$

$$\psi_2^c = 3\frac{(2\pi)^2}{a^3}\sum_{\mathbf{q}=\mathbf{g}}|S(\mathbf{q})|^2 e^{-Aq^2}\frac{(1 - F(q^2))^2}{q^4}\frac{\delta^2 q_t^2(q_l - \delta)}{q_l^4},$$

with $a$ being the lattice constant. The superscripts $i$ and $c$ denote the incoherent part and coherent part, respectively. We used $A$ for the thermal oscillation constant

$$A = \frac{3m_e^2 c^2}{4M K_B \Theta_D}[1 + 4(\frac{T}{\Theta_D})\Gamma(\frac{\Theta_D}{T})], \qquad (8)$$

11

where $M$ is the atomic mass of the crystal, $K_B$ is the Boltzmann constant, $\Theta_D$ and $T$ are the Debye temperature and the absolute temperature of the crystal respectively. We also introduced the structure factor $S(\mathbf{q})$ which accounts for the interferencial effect coming from the periodic nature of the crystal. The summation in the coherent part should be done over the reciprocal lattice points $\vec{g}$ kinematically allowed, *i.e.* mainly those in the *pancake* region.

## 2.2   Dip-bump structures

We show in the following the qualitative behavior of the differential cross section. For most conditions, the incoherent part depends weakly on $x$ and is a slowly varying function of $k$. On the other hand, the coherent part depends strongly on both $x$ and the direction of the crystal.

We first investigate the case where the incident electron enters parallel to one of the crystal axes, [110]*. For the lower boundary of the pancake to reach the first row of reciprocal lattice points, $\delta$ is equal to $\sqrt{2} \times 2\pi/a = 9.6 \times 10^{-3}$ in the case of silicon crystal. Choosing $E_0 = 1.2\text{GeV} = 2.3 \times 10^3$ in the present unit, we find that the corresponding $x$ is 0.98. This is very close to the end of the spectrum, where the momentum transfer is so large that the intensity of coherent contribution is very small with respect to the incoherent one. The cross section has therefore no appreciable enhancement in the coherent part.

Next, we consider the case where the incident electron enters the crystal with a small angle $\Theta$ with respect to the axis [110]* as seen in Fig. 3(a). Now, for a certain photon energy $k_0$, the pancake intersects the (110) plane, as shown in Fig. 3(b). This gives a large enhancement in the cross section.

12

$[001]^*$

(a)

$\mathbf{p_0}$

$\theta$

$\dfrac{2\pi}{a}$

$[110]^*$

$\sqrt{2}\dfrac{2\pi}{a}$

$\delta$ $\delta$

$[001]^*$

(b)

$[1\bar{1}0]^*$
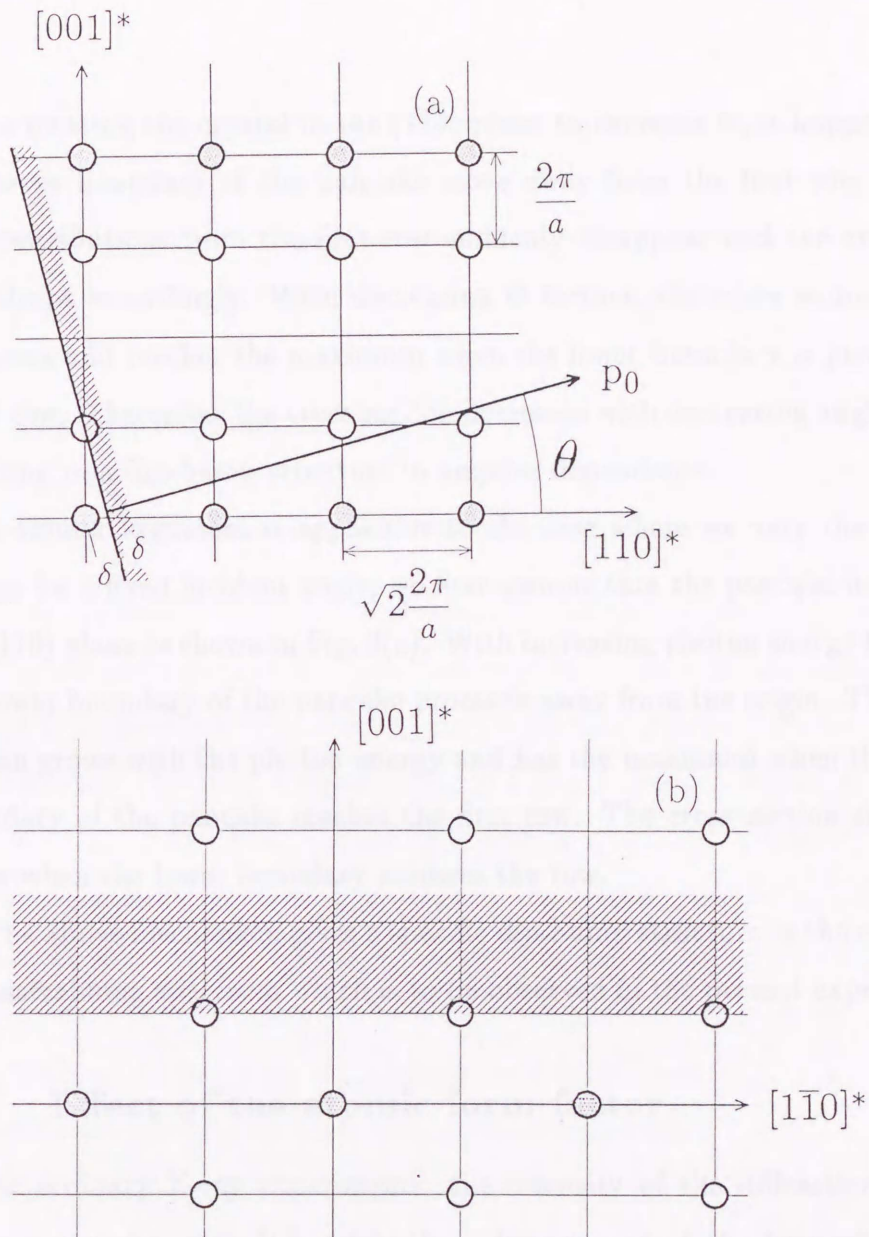
Figure 3: (a) The direction of the incident electron momentum $\mathbf{p_0}$ is directed through a small angle $\Theta$ in the plane $(1\bar{1}0)$. (b) The pancake now includes the reciprocal lattice points in the (110) plane.

While rotating the crystal in the ($1\bar{1}0$) plane to decrease $\Theta$, it happens that the lower boundary of the pancake move away from the first row. Then, the contributions from the first row suddenly disappear and the cross section drops accordingly. With decreasing $\Theta$ further, the cross section again increases and reaches the maximum when the lower boundary is just on the third row. Thereafter the cross section decreases with decreasing angle, thus, resulting in a dip-bump structure in angular dependence.

A similar argument is applicable to the case where we vary the photon energy for a fixed incident angle; we first assume that the pancake intersects the (110) plane as shown in Fig. 3(a). With increasing photon energy from $k_0$, the lower boundary of the pancake proceeds away from the origin. The cross section grows with the photon energy and has the maximum when the lower boundary of the pancake reaches the first row. The cross section suddenly drops when the lower boundary acrosses the row.

The above mechanism gives a specific dip-bump structure in the coherent bremsstrahlung spectrum which is to be observed in the present experiment.

## 2.3   Effect of the atomic form factor

In the ordinary X-ray experiments, the intensity of the diffraction image is proportional to $|F(q^2)|^2$, while the coherent part of the bremsstrahlung spectrum is proportional to the factor $(1 - F(q^2))^2/q^4$.

The discussion of the previous section shows that the specific dip-bump structure of the coherent bremsstrahlung comes from the lattice structure of the crystalline target and that the intensity of the spectrum is inversely pro-

14

portional to the fourth power of the momentum transfer which corresponds to the distance in the reciprocal lattice space. Now, it is clear that a possible small deviation in the atomic form factor at small momentum transfer may result in a large deviation in the coherent bremsstrahlung intensity.

# 3 Experimental Set-up

## 3.1 General consideration

There are several methods to determine the energy of photons emitted in the bremsstrahlung process. The first one is to measure the momenta of $e^+$ and $e^-$ pair which is converted from a photon, which is known as pair-spectrometry. In this method, though a good energy resolution can be achieved, the time needed to get the photon spectrum is huge. Another direct-measurement method is to convert the photon to an electromagnetic cascade shower. To get a good accuracy, we must keep the intensity of the photon beam to be such low that the only one photon will enter the detector in one trigger signal. The data amount to a large magnitude and the time needed to get one photon spectrum is accordingly long.

Instead of these direct measurements, we adopt the following indirect method: if we know both the energy of the incident electron, $E_0$, and that of the final electron, $E$, we can determine the photon energy $k$ by the relation $k = E_0 - E$. We place an analyzer magnet downstream the target. The electron which emits a photon has a smaller curvature in the magnetic field compared with the electrons which do not emit any photon and therefore

appears at different exit point of the analyzer magnet. We place a counter hodoscope downstream the analyzer magnet and measure the momentum of a recoil electron by its hit position on the hodoscope. This method is called the tagging method because the energy of all the photons is tagged by the momentum of the recoil electron. As we do not need to identify the individual photons, we only count the number of the recoil electrons which hit and of counter elements of the hodoscope. The counting rate in this case can be increased until it reaches to the limiting counting rate for single electrons.

As the characteristic feature of the coherent bremsstrahlung appears in the lower photon energy region, we mainly confine ourselves to employ a hodoscope which can measure high-energy recoil electrons..

Since we had to remove the error due to the differences in the energy acceptances for different counter elements of the hodoscopes, we took the ratio of each spectrum to the standard one which was obtained for the polycrystalline aluminum target under the standard conditions. Hereafter, this ratio is referred to as the normalized spectrum.

As it is difficult to extract beam with high enough stability and to make a direct measurement of beam intensity upstream of the target without disturbing the beam properties, we count the number of electrons of 1.2 GeV by a thick-walled ionization chamber placed downstream the analyzer magnet.

To vary the direction of the crystalline target relative to the incident electron beam, we use a high-precision goniometer which is controlled by a personal computer at the counting room.

16

## 3.2 Electron synchrotron

The electron synchrotron and the tagging system at the Institute for Nuclear Study, University of Tokyo, was used[15] in this experiment. The circulating electrons lose their energy in an absorber and are kicked out to the external beam line by two fast kickers. The beam line is schematically shown in Fig. 4. It has two lead slits that can collimate the electron beam in both vertical and horizontal directions.

At the first collimator, the beam is scraped to ±1mm in both vertical and horizontal directions. The secondary electrons which are created at the first collimator are scraped out by the second collimator. The quadrupole magnets are tuned to make the beam divergence at the target position as small as possible.

## 3.3 Tagging system and electron monitor

The tagging system consists of the analyzer magnet and two counter hodoscopes as shown in Fig. 5. The magnet supplies a magnetic field of 1.17 T and an effective field length of 0.8 m. The high-energy electrons from the accelerator, after hitting a target material, enter this magnetic field and give their trajectories according to their momenta.

There are two kind of counter hodoscopes of plastic scintillators. One is for low-energy electrons, the other is for high-energy ones. The spread of the electron beam due to the multiple scattering in the target material is not negligible because the analyzer magnet is horizontally defocusing. In the case of 0.5 mm silicon target, the spread of the beam at the hodoscope is

17
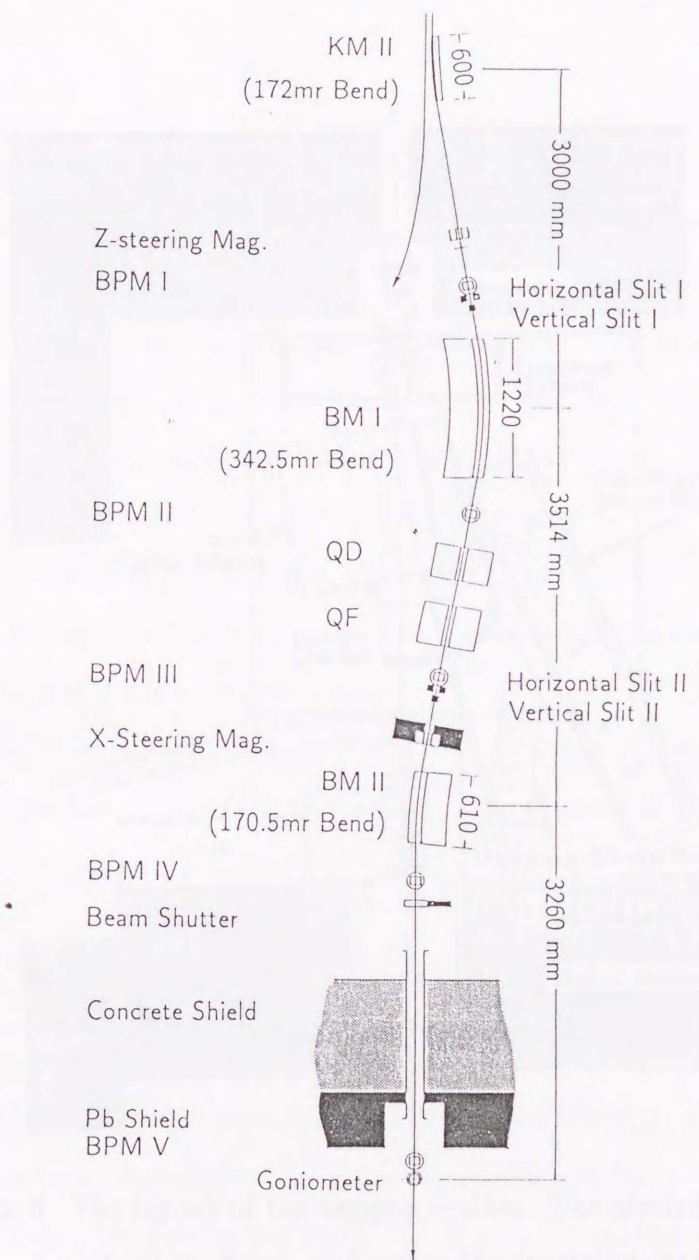
Figure 4: The layout of the electron extraction beam line. BM : bending magnet. KM : pulsed kicker magnet. BPM : beam profile monitor.
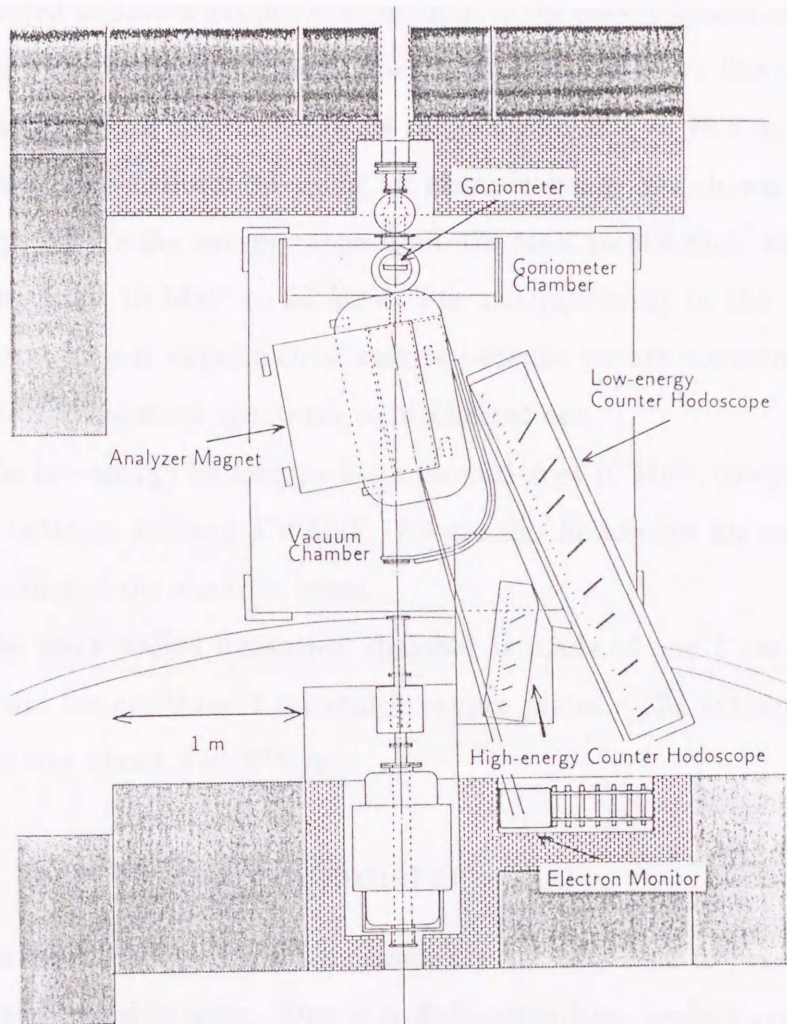
Figure 5: The layout of the tagging system. The electron beam comes from the upper side of the figure and enters the crystalline target on the goniometer. Electrons are analyzed according to their momenta by an analyzer magnet. There are two sets of counter hodoscope. Downstream the analyzer magnet, there is a thick-walled ionization chamber which counts the number of extracted electrons.

19

calculated to have a width corresponding to the energy spread of 20 MeV. We designed the energy acceptance of each bin to be 20 MeV. The corresponding horizontal size of the scintillators ranged from 10.6 to 19.0 mm.

An energy calibration using an electron beam has shown that the hodoscope covers the energy range from 975 MeV to 600 MeV with bin width ranging from 15 MeV to 20 MeV. The nonuniformity in the acceptance is irrelevant to our experimental results because we are concerned only with the ratio of coherent spectrum to incoherent one.

The low-energy hodoscope has a resolution of 10 MeV, covering an energy range between 100 and 370 MeV. We use this hodoscope for calibration and monitoring of the electron beam.

The thick-walled ionization chamber is made of one 2 cm-thick copper wall, and twenty-three 1 mm-thick copper plates. The extracted beam intensity was about $2 \times 10^8 \mathrm{e}^-/\mathrm{s}$.

## 3.4 Target and goniometer

Two kinds of high-purity silicon single crystal were used to observe the effect of crystal imperfectness. One is a dislocation-free, perfect crystal and the other is a crystal which has dislocation with a density of $\sim 10^4 \mathrm{cm}^{-2}$. They have been provided by Shin-etsu Handoutai Co. Ltd. It is hard to introduce dislocations heavier than in the present case into a silicon crystal without making cracks.

The silicon crystals used in the experiment were wafers with a thickness of 0.5 mm and a dimension of 20 mm×20 mm. The surface of the target crystal

20

is (110) and the edges are parallel to [$\bar{1}11$] and [$1\bar{1}2$] within an accuracy of 0.5°. The orientation of the target crystal was determined by the back reflection Laue method.

The goniometer has three axes which cross at one point and one translational moving axis as shown in Fig. 6. Around each axis, rotation is made
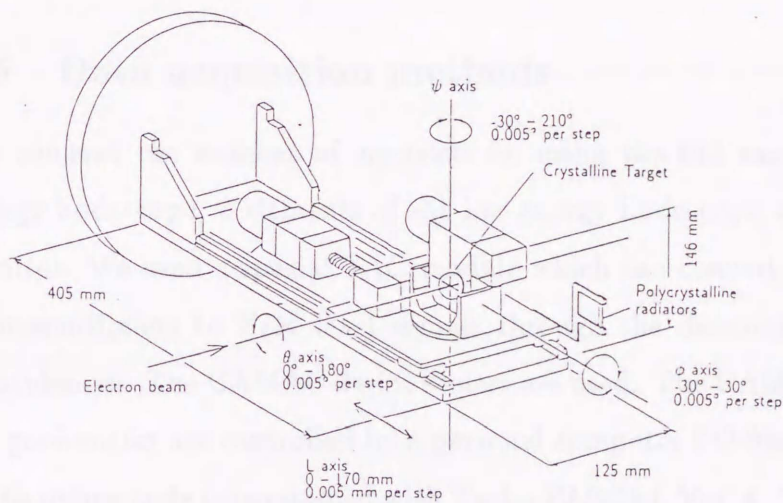


Figure 6: Whole view of the goniometer. It has three axes which cross at one point each other. It is placed in a vacuum chamber.

by a stepping motor in vacua and the position is informed through rotary encoders. The possible range of rotation is −30.000° ∼ 210.000° for the $\psi$ axis, −30.000° ∼ 30.000° for the $\phi$ axis and 0.000° ∼ 180.000° for the $\theta$ axis with a common precision of 0.005°. The crystalline target is mounted on a holder which has a circular opening window of 20 mm in diameter for the beam. The crystal must therefore be larger than 20 mm at least in one direction to bee mounted on the holder.

21

Sliding the goniometer transversal to a beam line, we can use a poly-crystalline material as the target. The polycrystalline radiators used are a 0.5 mm thick aluminum strip, an aluminum wire of 0.5 mm in diameter and a 50 $\mu$m-platinum strip. The frame of these targets is far from the beam and has no appreciable contribution to the spectrum.

## 3.5 Data acquisition methods

We counted the number of electrons by using the full range of the high-energy hodoscope, 8 elements of the low-energy hodoscope and the electron monitor. We used a special TAG module which can convert the signal from photomultipliers to NIM level signals through the discriminators and the coincidences. The CAMAC 24-bit scalers are used. The CAMAC system and the goniometer are controlled by a personal computer PC-9801RA4 with use of the online code programmed with Turbo PASCAL Ver. 4. The goniometer and the scaler were computer-controlled . The temperature of the crystal holder of the goniometer was monitored by three thermistors.

# 4   Experimental Procedure

## 4.1   Check runs

The number of data sets obtained in this experiment is summarized in Table 1.

To estimate the contribution of the secondary electrons produced in the beam line to the main spectrum, we measured the energy spectrum of elec-

22

| Run name | $\psi axis$ | | Number of data |
|---|---|---|---|
| Completely empty | | | 15 |
| Empty holder | | | 200 |
| Normalization run | | | 20 |
| Perfect Si | | check run | 910 |
| | $[001]^*$ | search | 850 |
| | $[001]^*$ | high statistics | 330 |
| | $[\bar{1}10]^*$ | search | 720 |
| | $[\bar{1}10]^*$ | high statistics | 70 |
| Imperfect Si | | check run | 340 |
| | $[001]^*$ | search | 270 |
| | $[001]^*$ | high statistics | 60 |
| | $[\bar{1}10]^*$ | search | 770 |
| | $[\bar{1}10]^*$ | high statistics | 90 |
| Aluminum run | | check run | 9600 |
| | $[\bar{1}10]^*$ | search | 800 |
| | $[\bar{1}10]^*$ | high statistics | 70 |
| | $[001]^*$ | search | 800 |
| | $[001]^*$ | high statistics | 60 |

Table 1: The number of data obtained in this experiment

23

trons with the target removed. Two types of *empty runs* were carried out occasionally. The first type is *completely empty* runs whose data are taken at the transverse position of the goniometer completely far away from the beam line. The obtained ratio of the spectrum for the *completely empty* to that for A$\ell$ target ranged from 0.6% to 1% for the high-energy hodoscope and 1.5% to 4% for the low-energy hodoscope.

The other is *empty holder* run for which we set the goniometer at the normal position but without target crystal. Because the opening window of the holder is not large enough to avoid the contribution from the beam halo, the obtained empty ratio is larger than that in the *completely empty* case. The ratio in this case to the A$\ell$ spectrum amounted to $3 \sim 4.5\%$ and $9 \sim 11$ % for high- and low-energy hodoscopes, respectively. We preformed *completely empty* runs and *empty holder* runs 7 times each.

We used the incoherent bremsstrahlung spectra for a calibration of the energy acceptance of the tagging channels and for the checking of the reliability of the system. The polycrystalline target of 0.5 mm-aluminum strip with a thickness of 0.5 mm was used for this purpose. Since the beam condition might change in time, the incoherent bremsstrahlung runs were preformed from time to time, 7 times in total. The spectra of two adjacent incoherent runs were found to be the same within a deviation less than 0.1%. The incoherent bremsstrahlung spectra from an aluminum strip measured in 10 s is shown in Fig. 7.
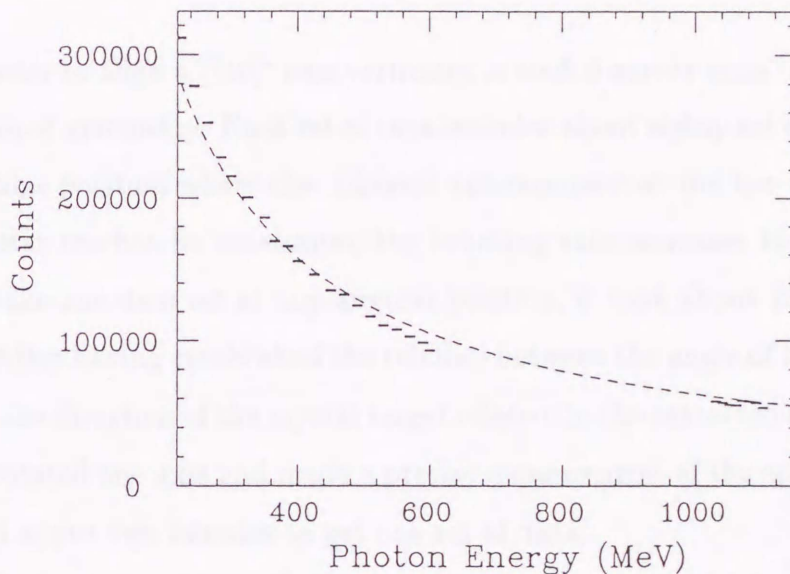
Figure 7: The incoherent bremsstrahlung spectrum measured in 10 s from the Aℓ polycrystalline radiator. The errors are due to statistics only. The dashed curve is the fitted 1/k curve.

## 4.2 Silicon runs

We mounted the crystalline target on the holder in such a way that the (110) plane of the crystal faced to the incident beam with one edge of [$\bar{1}$11] directed to the vertical when both of the goniometer angles $\phi$ and $\theta$ is 0°. By rotating the target around the $\theta$ axis, the symmetry axis was made to be parallel to the $\psi$ axis. The symmetry axes we have chosen were [$\bar{2}2\bar{1}$]*, [$\bar{1}$10]* and [001]*.

First, rotating one axis while leaving the others unchanged, we observed the orientational dependence of the spectrum and searched for the symmetry center. Next, fixing this temporary symmetry center, we rotated the target around the other axis and searched for another symmetry center. We repeated this process until we confirmed the two symmetry axes. For example,

25

in order to align a $[\bar{1}10]^*$ axis vertically, it took 5 survey runs to establish the required symmetry. Each set of runs includes about eighty set of data. At the angular position where the coherent enhancement at the low photon-energy counter reaches its maximum, the counting rate increases to 80k counts/s. To take one data set at any angular position, it took about 10 seconds.

After having established the relation between the angle of the goniometer and the direction of the crystal target relative to the extracted electron beam, we rotated one axis and made a precise measurement of the spectrum, which need about two minutes to get one set of data.

The spectrum from the imperfect silicon crystal is obtained in a manner completely similar to the perfect silicon case.

## 4.3 Aluminum runs

The aluminum single crystal used in this experiment was a 24 mm×5 mm strip of 0.5 mm thickness which was grown up by means of strain-annealing method. The purity was 99.999 %. The face of the strip was about 3° from the (110) crystal plane and longer edge directed to $[001]^*$.

The crystalline target was mounted on the holder in such a way that the (110) plane of the crystal faced to the incident beam with longer edge of $[001]^*$ directed to the vertical when both of the goniometer angles $\phi$ and $\theta$ is 0°. The symmetry axes we have chosen were $[\bar{1}10]^*$ and $[001]^*$.

The spectrum is obtained in a manner similar to the silicon case. As the dislocation density of the aluminum crystal was far heavier than that of silicon one, we spend long time to search for the good place on the crystal

26

by moving the incident beam or L axis of the goniometer.

In Fig. 8 the orientational dependence of the normalized spectrum for aluminum crystal is shown. The farthest peaks from the symmetry center correspond to the enhancements when the pancake region intercepts the reciprocal lattice points on the line defined by $\bar{1}11$ and $\bar{1}1\bar{1}$. The second peaks correspond to the line of $\bar{2}22$ and $\bar{2}2\bar{2}$, and so on.
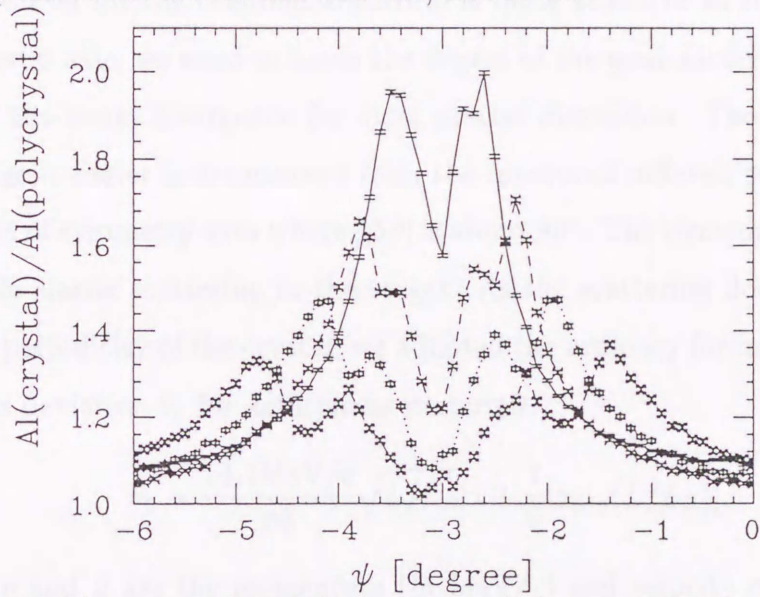


Figure 8: The orientational dependence of the normalized spectra of aluminum crystal. The symmetry axis is [001]. The photon energies are 245 (solid curve), 365 (dashed), 490 (dotted) and 600 MeV (Dot-dashed).

# 5 Results and discussion

## 5.1 Theoretical calculation

We compare the present experimental results with the theoretical calculations which employ Eq. (7) and various types of form factors. Since the differential cross section for the coherent spectrum is quite sensitive to the direction of the crystal axis, we need to know the degree of the goniometer misalignment and of the beam divergence for more precise discussion. The misalignment of the goniometer is determined from the measured differences between two position of symmetry axes where $|\Delta\theta|$ is about 90°. The electrons undergo the multiple elastic scattering in the target. As the scattering does not depend on the periodicity of the crystal, we adopted the ordinary formula for average angular deviation $\theta_0$ for amorphous materials:

$$\theta_0 = \frac{14.1\mathrm{MeV}/c}{p\beta}\sqrt{L/L_R}[1 + \frac{1}{9}\log_{10}(L/L_R)], \qquad (9)$$

where $p$ and $\beta$ are the momentum (in MeV/$c$) and velocity of the incident particle, respectively, and $L/L_R$ is the thickness, in units of radiation length of the scatterer. Since the scattering effect has azimuthal symmetry, we get the same multiple scattering divergence $\delta\theta_m = 0.0368°$ in both horizontal and vertical directions. With the beam divergence of $\delta\theta_b = 0.009°$ in both direction, we finally get the total directional divergence of the beam using the following relation:

$$(\delta\theta)^2 = (\delta\theta_b)^2 + (\delta\theta_m)^2,$$

which leads to $\delta\theta = 0.0379°$ for both $\psi$ and $\phi$ directions. In the calculation, we summed spectra from the 10 angular values for both vertical and horizontal directions with the Gaussian-type weight whose standard deviation is given by $\delta\theta$.

In order to take into account the effect of the energy acceptances of the counter hodoscope, we calculate the differential cross section for the three photon energies $\Delta E = E - E_{set} = -7, 0$ and $+7$ MeV for each energy bin, and then took the mean of the results for these three points.

We make an ellipsoid of revolution that contains normal pancake region completely to choose the reciprocal lattice points which contribute to the spectrum in the calculation. It is insufficient to count the reciprocal lattice points only in the normal pancake region to attain an accuracy high enough to distinguish the difference between the form factors because the longitudinal momentum transfer has no upper limit. We added a few more points out of the ellipsoid and checked the magnitude of their contribution. The upper limit point we adopted has a contribution of at most $5 \times 10^{-5}$ of that of the boundary points in the ellipsoid.

The measured temperature near the crystal holder was from 30°C to 40°C due to the heat transfer from the stepping motors of the goniometer. As the Debye temperature of silicon is high enough, the variation of the temperature contributes very little in the present case. We have chosen a temperature of 40°C in the calculation.

The incoherent bremsstrahlung spectrum for the aluminum target is given in a published table[4]. We finally obtain the result in a form of (spectrum from the crystalline target) / (spectrum from the polycrystalline target).

## 5.2 Atomic form factor of silicon crystal

Since the crystal holder of crystalline target partially intercepts the beam halo, we correct the data for the crystalline target by using the *holder empty* data. In the case of the data for polycrystalline target, the contribution from the target holder is negligible. We compensated the data for the polycrystalline target using the results of *completely empty* runs.

We show the orientational dependence of the normalized spectrum on several selected counters of the hodoscopes in Fig. 9(a) for the perfect silicon where the $\phi$ axis is set at the symmetry center, $\phi = -1.756°$. The abscissa is the angle $\psi$ of horizontal rotation, while the ordinate is the ratio of counts (crystalline silicon)/(polycrystalline aluminum) normalized to the same count of the electron monitor. The error bars are due to statistical effects only. We clearly see the symmetric behavior with respect to the crystal axis [110]* and this behavior has a good reproducibility. The farthest peaks from the symmetry center correspond to the enhancements when the pancake region intercepts the reciprocal lattice points on the line defined by $\bar{1}11$ and $1\bar{1}1$. The second and the highest peaks correspond to the line of $\bar{1}13$ and $1\bar{1}3$, and so on. The peaks move with photon energy, being consistent with the theoretical prediction in section 2.

Fig. 9(b) shows the orientational dependence of the normalized spectrum for the imperfect silicon crystal where the $\phi$ axis is set at the symmetry center $\phi = -0.978°$. Almost the same structure as in the case of perfect silicon can be seen.

Very close to the symmetry center, $\psi_c = 2.299°$ for the perfect silicon in
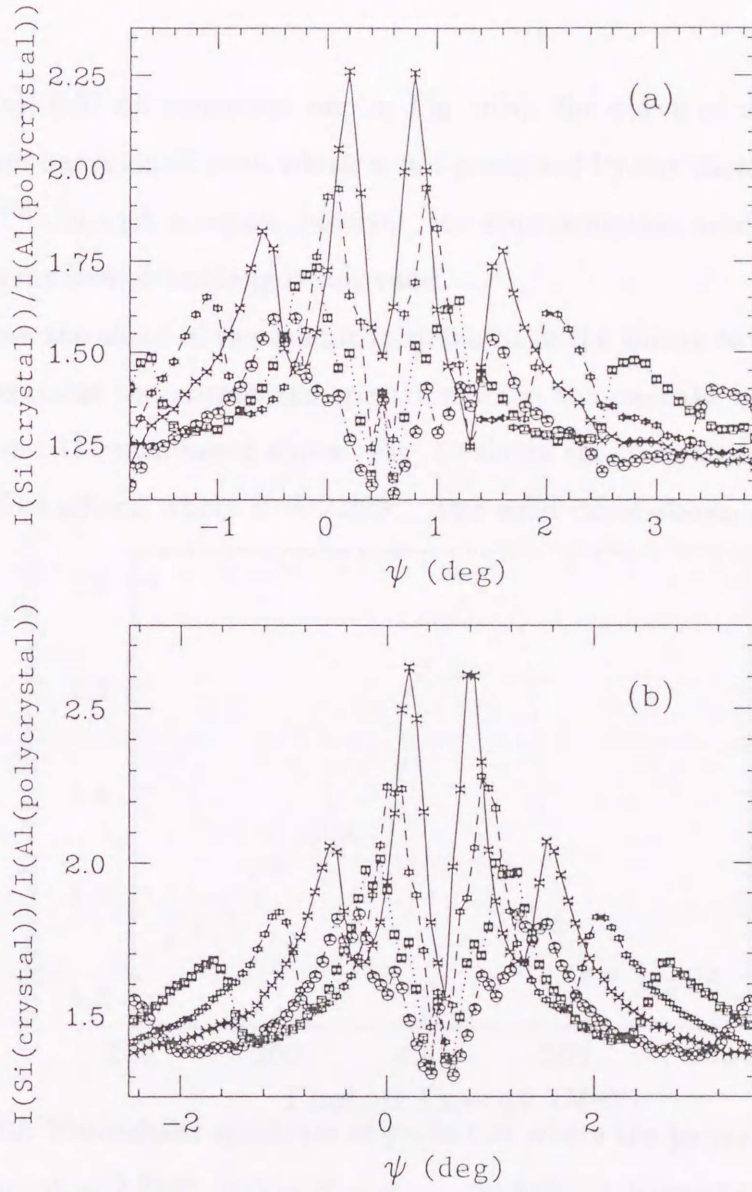
Figure 9: The orientational dependence of the normalized spectra of (a) perfect Si crystal and (b) imperfect Si. The abscissa is the horizontal rotation $\psi$. The symmetry axis is $[\overline{1}10]$. The photon energies are 300 (solid curve), 400 (dashed), 510 (dotted) and 600 MeV (dot-dashed). The error bars are due to statistics only.

Fig. 9(a), 0.5° for imperfect one in Fig. 9(b), the curve of the normalized spectrum has a small peak which is not predicted by the theory as reported earlier[16]. In such a region, however, the approximation used in the theory of coherent bremsstrahlung is not valid.

To see the effect of the atomic form factor of the silicon to the spectrum, let us examine the normalized spectrum when the pancake is near the line of $\bar{1}11$ and $1\bar{1}1$ mentioned above. Fig. 10 shows the normalized spectrum of the perfect silicon where $\psi = 2.299°$. The solid curve shows the calculated
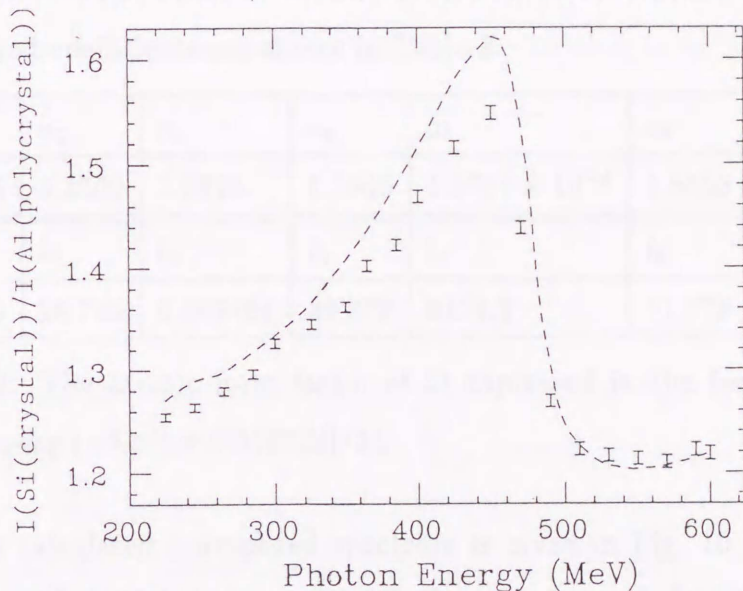


Figure 10: Normalized spectrum of perfect Si where the pancake is near the $[\bar{1}11]$ line, $\psi = 2.299°$, $\Delta\psi = \psi - \psi_{center}$ is 1.8°. A theoretical calculation based on Hartree-Fock model are also shown by the dashed curve.

spectrum for the Hartree-Fock form factor[2]. and there is a good agreement between the experimental and the theoretical curves besides a slight difference near the peak of the normalized spectrum, where the theoretical curve

lies below the experimental data. This behavior is kept unchanged during the experiment and hence not due to the radiation damage effect.

The experimental results for the perfect silicon are compared with the calculations which employ the Hartree-Fock (HF) form factor[2]. In order to simplify our calculation, we expand the form factor in the following form by means of least-sqare method:

$$F(q^2) = \sum_i^7 a_i \exp(-b_i q^2) + c. \tag{10}$$

The fitted coefficients are shown in Table 2.

| $a_1$ | $a_2$ | $a_3$ | $a_4$ | $a_5$ | $a_6$ | $a_7$ |
|---|---|---|---|---|---|---|
| 7.4456 | 3.3509 | 1.6818 | 1.5049 | $1.3791 \times 10^{-4}$ | $1.5653 \times 10^{-4}$ | $1.3791 \times 10^{-4}$ |

| $b_1$ | $b_2$ | $b_3$ | $b_4$ | $b_5$ | $b_6$ | $b_7$ |
|---|---|---|---|---|---|---|
| 1.9520 | 28.745 | 0.069804 | 89.377 | 9114.2 | 51.779 | 9994.0 |

Table 2: The atomic form factor of Si expressed in the form of $F(q^2) = (\sum_{i=1}^7 a_i \exp(-b_i q^2) + 0.018712)/14$

The calculated normalized spectrum is given in Fig. 10 by the dashed curve, which is to be compared with the experimental data for the angular divergence being $\Delta\psi = 1.8°$ and $\Delta\phi = 0°$ with respect to the symmetry axis. The experimental data lie somewhat lower than the HF curve near the peak of the spectrum. It is, however, difficult to regard the difference observed between experimental data and the calculation as due to the inadequacy of the form factor used because the theoretical treatments we have adopted has uncertainties of the order $\alpha = 1/137$, the fine structure constant, whereas the

33

observed difference is also of this order. It may be a systematic error in the theoretical calculation. On the other hand, if we assume that the difference is due to the deviation in the atomic form factor, the resulting form factor should be slightly increased in comparison with the HF.

The form factor of Si crystal is known to an accuracy of 0.05% from the measurement with the *Pendellösung* method by Saka and Kato[10]. They showed that the form factor of 111 reflection, the lowest reflection, has the largest deviation from the HF form factor. In our case, since the calculated curve is the sum of the contribution from many reciprocal lattice points, it is generally impossible to uniquely determine which part of $F(q^2)$ is to be modified. We first follow the result from Saka and Kato. We have tried to fit our results adding the following extra Gaussian term

$$a \frac{1}{\sqrt{2\pi}\sigma} exp(-\frac{1}{2}\frac{(q-\mu)^2}{\sigma^2}),\qquad(11)$$

of which standard deviation is $\sigma = 0.02\text{Å}^{-1}$. We first fixed the center of the extra Gaussian to the 111 ($\mu = 0.16\text{Å}^{-1}$) and varied the height $a$ to reproduce our experimental result. Fig. 11(a) shows the result in the case of $a = 0.02$ whose form factor differs from the HF by about 3.3% at 111. The original HF form factor and the modified one are compared in Fig. 12 as functions of the momentum transfer. This modified form factor can reproduce the present experimental results very well.

If we change the center of the extra Gaussian to 220 point ($\mu = 0.26\text{Å}^{-1}$) keeping its height unchanged, the fit goes worse as shown in Fig. 11(b), implying that the 111 reflection mainly contributes to the enhancement. Both of the present analysis and that by *Pendellösung* method suggest the same

34
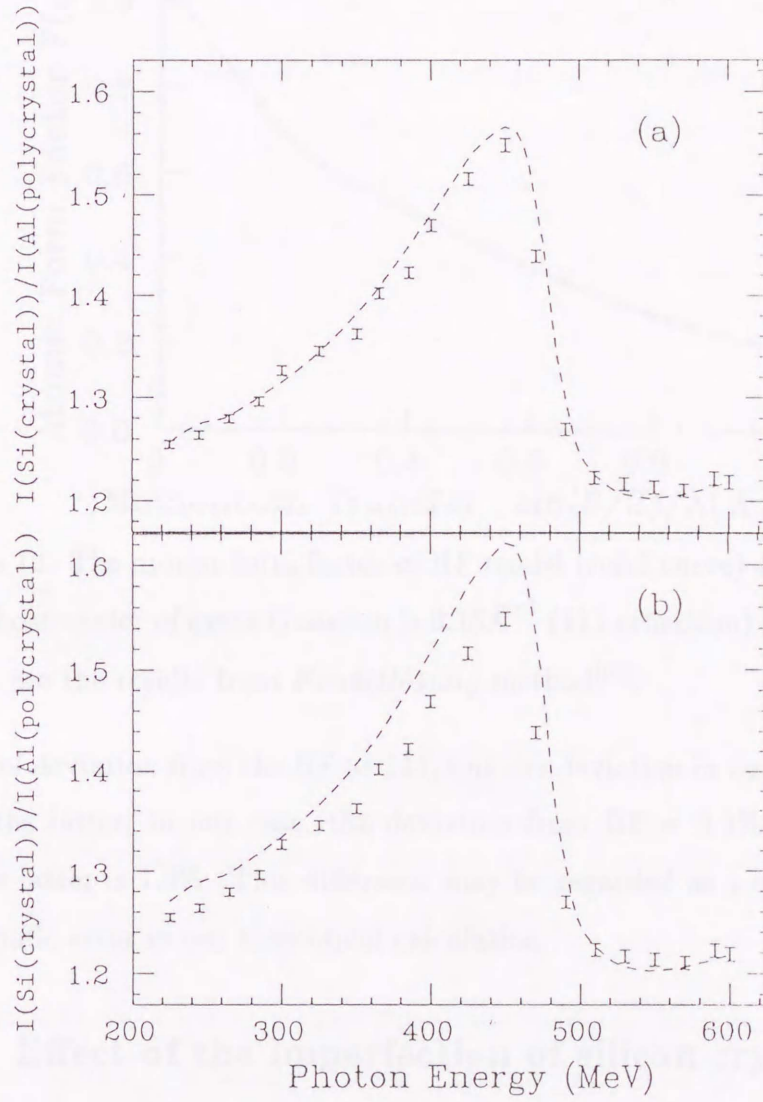
Figure 11: Normalized spectrum with the calculated result of which form factor is modified by adding an extra Gaussian (a) The extra Gaussian with $\mu = 0.16\text{Å}^{-1}$, $\sigma = 0.02\text{Å}^{-1}$, $a = 0.02$ is added. (b) The extra Gaussian with $\mu = 0.26\text{Å}^{-1}$, $\sigma = 0.02\text{Å}^{-1}$, $a = 0.02$ is added.
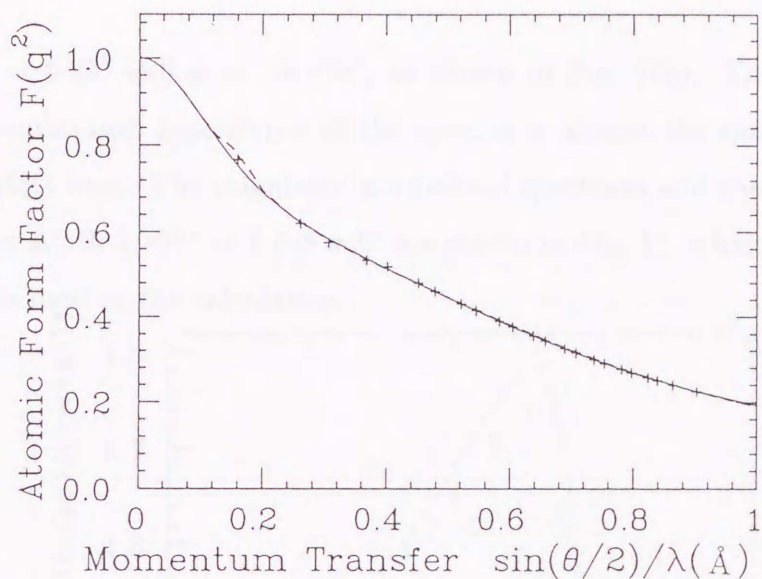
Figure 12: The atomic form factor of HF model (solid curve) and a modified one whose center of extra Gaussian is $0.16\text{Å}^{-1}$ (111 reflection) (dashed). The marks are the results from *Pendellösung* method[10].

trend of deviation from the HF at 111, but the deviation in our case is larger than the latter; in our case, the deviation from HF is 3.3% whereas that for the latter is 1.9%. This difference may be regarded as a consequence of systematic error in our theoretical calculation.

## 5.3   Effect of the imperfection of silicon crystal

If the target silicon has dislocation, the reciprocal lattice points become fuzzy. This is equivalent to increase the beam divergence for perfect silicon. This effect will reduce the normalized spectrum to some extent.

The spectrum obtained from the imperfect silicon target is analyzed by employing the same method as that for prefect one. The symmetry center

36

was $\psi = 0.55°$ and $\phi = -0.978°$, as shown in Fig. 9(b). The structure of the orientational dependence of the spectra is almost the same as that for the perfect ones. The calculated normalized spectrum and the experimental data for $\Delta\psi = 1.759°$ and $\Delta\phi = 0°$ are shown in Fig. 13, where the HF form factor is used in the calculation.
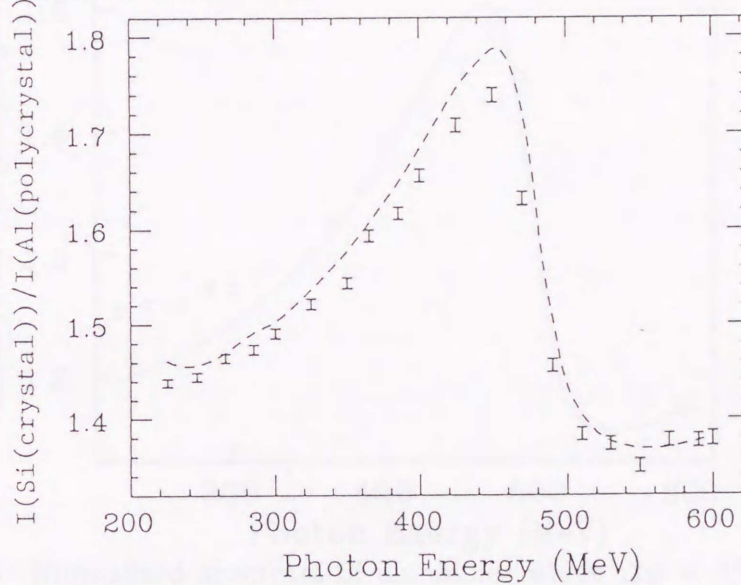


Figure 13: Normalized spectrum of imperfect Si under almost the same condition for the perfect one as shown in Fig. 10.

The difference between the theoretical curve and the experimental data in the vicinity of the peak is slightly larger than that for the perfect silicon. The difference between prefect and imperfect silicons is found to be so small that our method is applicable to such a metal crystal that has its dislocation density of the order of magnitude similar to that of the present imperfect silicon.

37

## 5.4 Atomic form factor of aluminum crystal

An example of energy spectrum is shown in Fig. 14 at an incident angle $\Delta\psi$ of $1°$, measured from the $[001]^*$ axis for the incident electron beam in the crystal plane (110). The error bars are due to statistical effect only. The solid curve
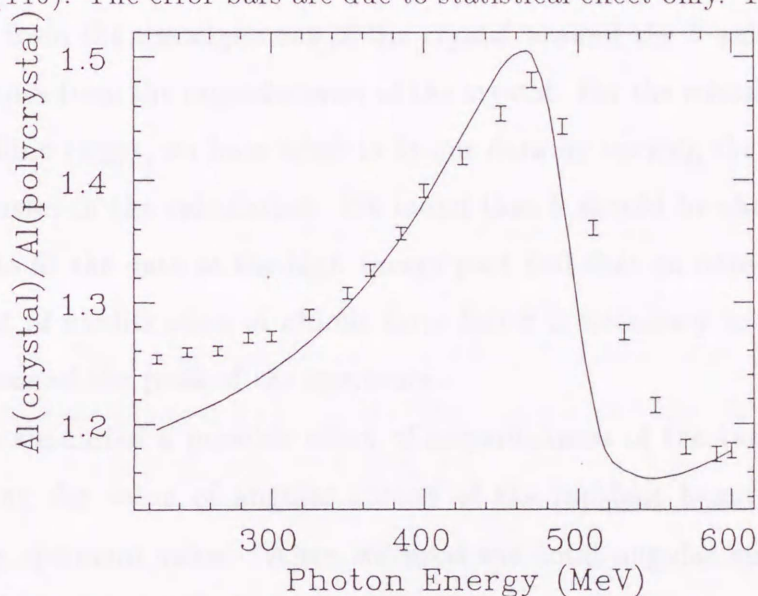


Figure 14: Normalized spectrum of aluminum where $\Delta\psi = 1°$. The error bars are due to statistical error only. A theoretical calculation based on Hartree-Fock model are also shown by the solid curve.

is a theoretical calculation with the atomic form factor based on the Hatree-Fock model (HF)[2] under the assumption of that the crystal is perfect and is oriented exactly to the desired direction. In this calculation we take into account the effect of the angular divergence and multiple scattering in the target material of the incident electrons together with the energy resolution. When the crystal temperature is varied from $30°$ to $60°C$, the calculated result shows no appreciable variation.

We see, in Fig. 14, that the experimentally observed peak is somewhat broader than the theoretical curve, which causes unacceptable disagreement around the high-energy side of the peak. There may be two possible origins of such softening of the peak structure in the experimental data; the first one comes from the misalignment of the crystal around the $\theta$ axis. The second one comes from the imperfectness of the crystal. For the misalignment of the crystalline target, we have tried to fit our data by varying the angle $\theta$ of the goniometer in the calculation. We found that $\theta$ should be changed by 4° in order to fit the data at the high energy part and that an unreasonably large amount of modification of atomic form factor is necessary to reproduce the data around the peak of the spectrum.

We simulated a possible effect of imperfectness of the target crystal by changing the value of angular spread of the incident beam and searched for the optimum value. When we used the total angular spread of 0.07°, instead of using 0.04° which is estimated from multiple scattering and beam divergence only, the shape agrees well with the data. In this case, we have found that relatively small change of the atomic form factor can reproduce the height of the spectrum.

In order to quantitatively demonstrate the sensitivity of the atomic form factor, we shown in Fig. 15 the calculated results for which $F(q^2)$ are modified by adding the extra Gaussian term of Eq (11). The standard deviation $\sigma$ and the height $a$ are arbitrarily chosen as $0.05\text{Å}^{-1}$ and $0.04\text{Å}^{-1}$, respectively. The solid, dashed and dotted curve corresponds the calculated results of which the mean of the extra Gaussian is at the reflection points of 111 ($\mu = 0.2116\text{Å}^{-1}$), 200($\mu = 0.2443\text{Å}^{-1}$) and 220($\mu = 0.3455\text{Å}^{-1}$), respectively. The amount of

39
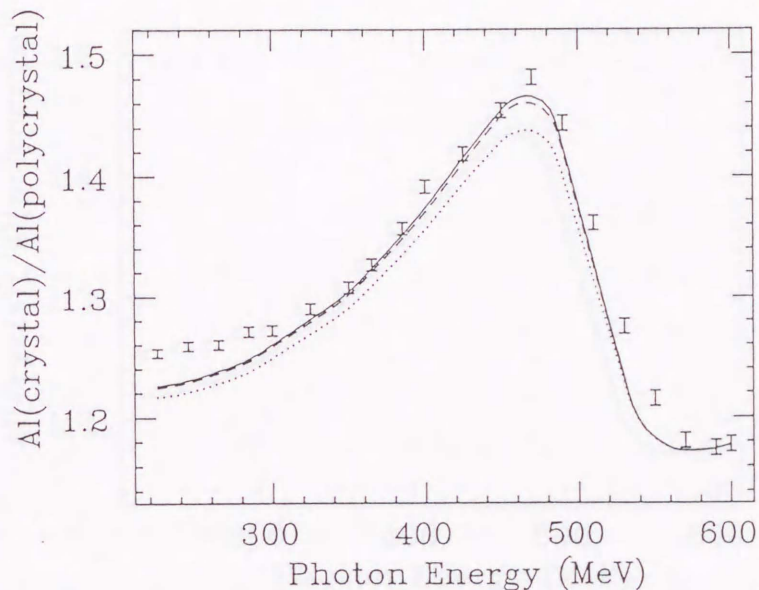
Figure 15: Normalized spectrum with the calculated result of which form factor is modified around 111 (solid), 200 (dashed) and 220 (dotted) reflection points by an equal amount.

modification of $F(q^2)$ is about -3.6% when selecting the 111 reflection point. Clearly the results are sensitive to the form factor of 111 and 200 reflections.

Since the calculated curve is the sum of the contribution from many reciprocal lattice points, it is generally impossible to uniquely determine which part of $F(q^2)$ is to be modified. Therefore, we only examine the adequacy of existing values of $F(q^2)$ obtained by x-ray measurements[17, 18, 19, 20, 21, 22] by putting them in our theoretical formula.

In Fig. 16 we show the calculated result using the $F(q^2)$ of 111, 200 and 220 reflections for HF[2], Takama[22] and Batterman[17] by solid, dashed and dotted curve, respectively. It is obvious that the calculation which uses the $F(q^2)$ of Batterman agrees with our data.

40
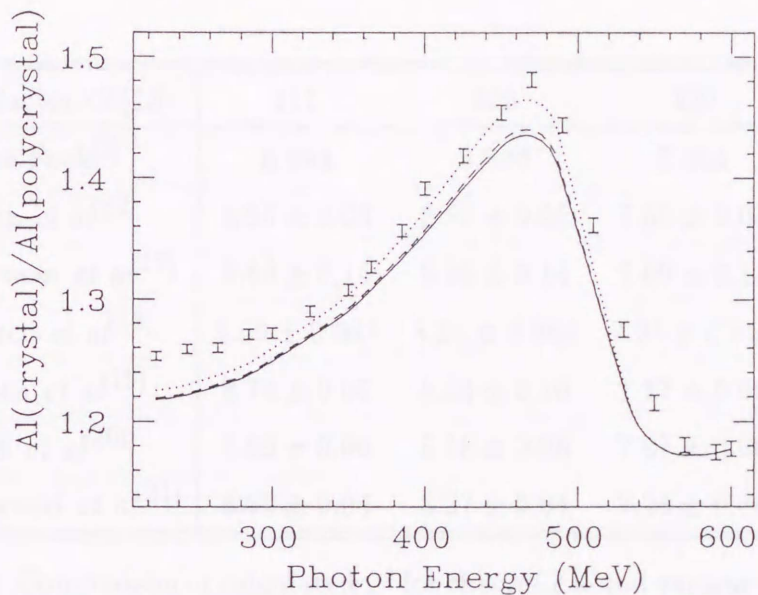
Figure 16: Normalized spectrum with the calculated result of which form factor is from HF[2] (solid), Takama[22] (dashed) and Batterman[17] (dotted).

To examine the fits of the calculated result to the data quantitatively, we introduce the value of $\chi^2$ which is defined by

$$\chi^2 = \sum_{i=1}^{20} \frac{(x_i - a_i)^2}{\Delta x_i^2},$$

where $x_i$, $\Delta x_i$ and $a_i$ are the experimental data, the statistical error and the calculated result for i-th energy bin, respectively. We show in Table 3 the calculated $\chi^2$ for the present experimental value of $F(q^2)$. Most of $\chi^2$ comes from inadequate treatment of low energy tail, where the sensitivity to form factor is negligibly small. It is, therefore, reasonable that the form factor with minimum $\chi^2$ is physically meaningful even though the $\chi^2$ per d.o.f is bad.

Our experimental result clearly supports a large modification, amounting to 4%, of $F(q^2)$ at 111 reflection as asserted by Batterman[17] and

41

| Form factor × Z(13) | 111 | 200 | 220 | $\chi^2$ |
|---|---|---|---|---|
| Hartree-Fock[2] | 8.994 | 8.540 | 7.364 | 772 |
| Takama $et\ al$[22] | $8.90 \pm 0.03$ | $8.52 \pm 0.05$ | $7.36 \pm 0.03$ | 670 |
| Batterman $et\ al$[17] | $8.63 \pm 0.14$ | $8.25 \pm 0.14$ | $7.09 \pm 0.13$ | 342 |
| DeMarco $et\ al$[18] | $8.69 \pm 0.043$ | $8.21 \pm 0.066$ | $7.25 \pm 0.058$ | 385 |
| Järvinen $et\ al$[19] | $8.74 \pm 0.06$ | $8.24 \pm 0.10$ | $7.17 \pm 0.09$ | 458 |
| Raccah $et\ al$[20] | $8.80 \pm 0.06$ | $8.38 \pm 0.06$ | $7.27 \pm 0.06$ | 525 |
| Rantavuori $et\ al$[21] | $8.80 \pm 0.04$ | $8.27 \pm 0.04$ | $7.24 \pm 0.04$ | 525 |

Table 3: Comparison of calculated $\chi^2$ for theoretical and various experimental values of $F(q^2)$. In this table, the atomic form factors for 111, 200 and 220 reflections are multiplied by atomic number Z=13.

DeMarco[18]. This suggests that, in the case of aluminum crystal, the electron density between the atoms is appreciably modified from that of an isolated atom.

## 5.5   Possible improvement of experimental methods

As discussed in the earlier section, the present set-up and the theory are enough to determine the atomic form factor of silicon to the level of few percents. Though this accuracy is insufficient for silicon but is readily useful for obtaining information of form factors for $A\ell$, to which we cannot apply the *Pendellösung* method completely.

The shortcoming of the present method is in the theoretical treatment which includes uncertainties of the order of $\alpha$, the fine structure constant,

implying that the comparison between calculated and experimental results is valid only to a few percent level. We need the terms of the second order in $\alpha$ to discuss the results within an accuracy of 0.5%.

In this experimental set-up, the beam cannot have the shape optimized for our experiment. As a results, the crystal must be thin and large in its perfect area. These constraints confine the kind of crystals to be measured in the present setup, but are not essential since use of more dedicated beam line can easily get rid of them.

# 6 Conclusion

We have developed a new method to determine the atomic form factor by means of precise measurement of the coherent bremsstrahlung. Counting the recoil electrons of Übeall effect, we obtained photon-energy spectra easily in a short time with strict reproducibility. The form factor was determined by modifying the HF form factor around the lowest reflection point so as to reproduce the experimental spectra. The change of experimental result due to the radiation damage of the target crystal was not observed. The shape of the coherent spectra from the silicon crystal has been reproduced excellently by a theoretical calculation which uses the HF form factor modified by about 3.3% at 111 reflection. This change qualitatively supports experimental results from *Pendellösung* method by Saka and Kato[10], although quantitatively the deviation from the HF in our case disagreed with that in the latter case by about 1.3%, which is just of the order of ambiguity in the theoretical calculations to be compared with our experimental results.

43

From these observations, if properly improved, the present method is much promising for high-precision determination of atomic form factor.

For the imperfect silicon crystal, we obtained a spectrum very similar to that for the perfect one. The difference is so small that we can apply the method to such a crystal that the dislocation density is of the order of $10^4 \mathrm{cm}^{-2}$.

The atomic form factor of aluminum crystal is determined by comparing the result of coherent bremsstrahlung with various experimental or theoretical atomic form factors. Our experimental result supports the atomic form factor obtained by the kinematical method as asserted by Batterman[17] and DeMarco[18] which clams large modification, amounting to 4%, of atomic form factor around 111 reflection from Hatree-Fock model calculation. The electron density of aluminum crystal between the atoms should be appreciably modified from that of isolated atom.

We conclude that our procedure has a good reliability and will be valid for many crystals. In addition, our final emphasis is that the present method enables us to obtain information complementary to that obtained from ordinary X-ray measurements.

## Acknowledgements

45

# References

[1] D. C. Creagh and J. H. Hubbell, Acta Cryst. **A43,** 102 (1987).

[2] D.T. Cromer and J.B.Mann, Acta Cryst. **A24** 321 (1968).

[3] J. A. Ibers, International Tables for X-Ray Crystallography, (Kynoch Press, Birmingham, England, 1962),**Vol.III**, 201.

[4] J. H. Hubbel *et al.*, J. Phys. Chem. Ref. Data, **4,** 471 (1975).

[5] D. Watanabe, R. Uyeda and M. Kogiso: Acta Cryst., **A24** 249 (1968).

[6] T. Kifune *et al.*, J. Phys. Soc. Japan,**21** 1905 (1966).

[7] G. Bologna, G. Lutz, H. D. Shultz, U. Timm, W. Zimmermann; IL Nuovo Cimento **A42**, 844 (1966).

[8] R. Voss, G. Lehmpfuhl and P. J. Smith, Z. Naturforsh. **35a,** 973 (1980).

[9] I. Endo *et al.*, Phys. Rev. Lett. **60,** 2292 (1988).

[10] T. Saka and N. Kato, Acta. Cryst. **A42,** 469 (1986).

[11] M. Hart: Z. Physik **189** 269 (1966).

[12] T. Takama and S. Sato: Aust. J. Phys, **41** 433 (1988).

[13] H. Bethe and W. Heitler, Proc. Roy. Soc. (London) **A146,** 83 (1934).

[14] U. Timm, Fortschritte der Physik **17,** 765 (1969).

[15] K. Yoshida *et al.*, IEEE Trans. Nucl. Sci. **32,** 2688 (1985).

[16] I. Endo *et al.*, Phys. Lett. A, **146** 150 (1990).

[17] B. W. Batterman, D. R. Chipman and J. J. DeMarco, Phys. Rev. **122**, 68 (1961).

[18] J. J. DeMarco, Phil. Mag., **15**, 483 (1967)

[19] M. Järvinen, M. Merisalo and O. Inkinen, Phys. Rev., **178** 1108 (1969)

[20] P. M. Raccah and V. E. Henrich, Phys. Rev. **184**, 607 (1969)

[21] E. Rantavuroi and V. P. Tanninen, Physica Scripta, **15**, 275 (1977)

[22] T. Takama, K. Kobayashi and S. Sato, Trans. Jpn. Inst. Metals, **23**, 153 (1982)

# 公 表 論 文

(1)Determination of atomic form factors by means of coherent bremsstrahlung
　（コヒーレント制動放射を用いた原子散乱因子の決定）
　M.Tobiyama, I.Endo, T.Monaka, Y.Sumi, H.Uchida, N.Yamamoto, K.Yoshida,
　K.Watanabe, T.Ohba, K.Baba and T.Emura
　Phys. Rev. B <u>44</u> 9248(1991)

(2)Determination of atomic form factor of aluminum by means of coherent
　bremsstrahlung
　（コヒーレント制動放射を用いたアルミニウム原子散乱因子の決定）
　M.Tobiyama, I.Endo, T.Kino, Y.Sumi, H.Uchida, N.Yamamoto, K.Yoshida,
　K.Watanabe, T.Ohba, K.Baba and T.Emura
　accepted for publication in Phys. Lett. A (1992)

# 参 考 論 文

(1)Determination of atomic form factor of silicon by means of coherent
   bremsstrahlung of 1.2 GeV electrons
   （1.2GeV電子からのコヒーレント制動放射を用いたシリコン原子散乱因子の決定）
   I.Endo, M.Harada, K.Kitamura, T.Monaka, Y.Sumi, M.Tobiyama, H.Tsujikawa,
   K.Watanabe, K.Yoshida, T.Ohba, K.Baba and H.Motegi
   Phys. Rev. Lett. 60 2292 (1988)

(2)Detection of recoil electrons in triplet photoproduction
   （3重電子光発生の反跳電子の検出）
   I.Endo, S.Kasai, M.Harada, K.Niki, Y.Sumi, M.Tobiyama, M.Mutou,
   H.Tsujikawa, K.Watanabe, K.Yoshida and K.Baba
   Nucl. Instrum. Meth. A280 144 (1989)

(3)Conceptual design of a 1.5-GeV x-ray ring
   （1.5GeVのX線領域まで使用可能な放射光リングの概念設計）
   M.Tobiyama, I.Endo, T.Ohta, T.Sugano and M.Taniguchi
   Rev. Sci. Insstrum. 60 1713 (1989)

(4)Suppression of Increase in Impurity in Single-Bunch Mode for the
   UVSOR Storage Ring
   （UVSOR電子蓄積リングの単バンチ運転での単バンチ純度悪化の抑制）
   M.Tobiyama, T.Kasuga, H.Yonehara, M.Hasumoto, T.Kinoshita, O.Matsudo,
   E.Nakamura, K.Sakai and J.Yamazaki
   Jpn. J. Appl. Phys. 29 210 (1990)

(5)Study of hard-photon emission from 1.2 GeV electrons in Si crystal
   （シリコン結晶中での1.2GeV電子からの高エネルギー光子放射の研究）
   I.Endo, T.Monaka, A.Sakaguchi, Y.Sumi, H.Uchida, N.Yamamoto, M.Tobiyama,
   K.Yoshida, K.Watanabe, T.Ohba, K.Baba and T.Emura
   Phys. Lett. A 146 150 (1990)

(6)Angular distribution of hard photons from 1.2 GeV channeling electrons
   in Si
   （シリコン中での1.2GeVチャネリング電子からの高エネルギー光子の角度分布）
   I. Endo, T.Tanioka, M.Tobiyama, H.Uchida, M.Muto, K.Yoshida, K.Watanabe,
   T.Ohba, K.Baba, T.Emura
   Phys. Lett. A 164 319 (1992)